Green University

GUBJSE: ISSN: 2409-0476

A_0-MODE LAMB WAVE BASED DETECTION OF CORROSION UNDER COATING FILM IN PLATE-LIKE METALLIC STRUCTURES: ANALYTICAL, FINITE ELEMENT AND EXPERIMENTAL STUDIES

M S Rabbi, and K Teramoto

***Abstract*—** The fundamental order antisymmetric mode (A_0-mode) Lamb wave based a quantitative acoustical imaging technique is proposed in this paper to classify the corroded region under coating film within the metallic structure. This method estimates versatility qualities of the zone of intrigue to some degree inhomogeneity differentiated to the encompassed materials. However, a converging region consisting of incident wave field and scattered wave field difficult to demonstrate from the observed signals. The proposed method focuses on reconstructing the image of the defect by calculating the shear strains. The shear strains deduced from the observed normal displacement of the specimen. A covariance matrix has been constructed using the shear strains and meaningful determinant values of the matrix reveal the overlapping region. As the beginning overlapping region developed at the edge of the defect, thus image of the defect can be reconstructed by this technique. This paper discussed the analytical approach of computing the incoming, outgoing, as well as the transmitting wave fields. Physical interpretation of the analytical prediction is explored via numerical simulations and acoustical observations.

***Index Terms*—** A_0-mode Lamb wave, out-of-plane displacement, shear strain, ultrasonic imaging

This paper was received on 22 April 2019, accepted on 20 August 2019.

M. S. Rabbi is with the Chittagong University of Engineering and Technology, Chattogram, Bangladesh. E-mail: *rabbi@cuet.ac.bd.*

K. Teramoto is now with the Department of Advanced Technology Fusion, Saga University, Japan. E-mail: *tera@me.saga-u.ac.jp.*

I. INTRODUCTION

IN the construction industry, employment of metal serve a wide scope of capacities. In view of the distinctive characteristics and proper uses, carbon steel, aluminum, stainless steel are the most well-known metal. Durability, strength as well as resistance to weather, offers the universal applications of metallic structure in both small and large scale. Detection of damage of these structures has been an important area of concern from the early stage of the product's lifecycle. Metallic structures may suffer from corrosion in a wide range of environments. After encountering such defect, investigation of such area is difficult to inspect because of limited access. Such kind of defect may cause the surface to blister, crack, or chip. Monitoring such type of damage in the structure can minimize maintenance cost and potential structure problem.

Lamb wave is widely acknowledged for last several decades as one of the most propitious quantitative damage identifying tools and has been studied intensively by various researchers worldwide for Structural Health Monitoring (SHM). With a significant susceptibility to inhomogeneity in a wave propagation path, Lamb waves can travel a long distance with a high attenuation ratio, and in this way a huge zone can be immediately inspected. Several pilot studies have long been recognized [1-3] as a eminent non-destructive evaluation (NDE) tool, as well as have been discussed by many authors [4-8]. Variable mode selection comprising with different combinations of incident angles and frequencies is the particular advantage of Lamb wave over the bulk wave. Lamb wave dispersion curve classically always exhibits two basic modes of propagation about the mid-plane of the plate, i.e. Symmetric (S) and Antisymmetric (A) [4]. It is examined that, fundamental order (S_0 and A_0) offers most effective for better resolution [9]. It was likewise presumed that S_0 shows sensible affectability to defects anyplace in the thickness, while A_0 is progressively touchy to corrosion or delamination [10]. The fundamental symmetric mode (S_0) is preferred in the majority of the studies [8,11-14], as this sort of wave takes into consideration the review of structures over sensibly long separations, and can be utilized if there should arise an occurrence of the neighbourhood access to that investigated part is beyond the realm of imagination. Utilization of A_0-mode is increasing as it has been illustrated that it is suitable for detecting transverse defect [15-19]. Conventional NDT technique has been utilized for undercoating corrosion

detection with the most effective being thermographic testing [20]. Several guided-wave based experiments have been carried out to detect the corrosion in the welded structure by Sargent [21-23]. NDE imaging by Terahertz under paint has been examined by reviewing the terahertz signal response to paint thickness and surface roughness [24]. The CUPID system has offered an extremely flexible and highly customized corrosion management system, which can detect the damage from remote place [25]. Lingyu et al. [26] presented the active corrosion detection technique in aluminum plate-like structure using time frequency analysis. A concept proposed by Rathod et al. illustrated the experimental results focusing on PWASs for corrosion detection in metallic plates [27]. Nagy et al. proposed a novel technique for suppressing the unwanted S_0-mode based on the Poisson effect of the material [28]. Chew et al. investigated the wall thickness reduction due to corrosion using high frequency guided ultrasonic waves propagating along the structure, quantifying the variation of wave interference in the frequency domain [29]. Sharma et al. reports a non-contact, *in-situ* corrosion monitoring technique for submerged plates using ultrasonic guided waves where along with the ultrasonic signal, mass-loss and stress strain behaviour and tensile strength of the plates at different stages of corrosion can be monitored [30]. Among a couple of investigations, the cross-time frequency analysis was found more reliable and precise compared to the statistical damage index method.

Ultrasonic imaging alludes to securing full waveform data over the interrogated region for waves generated by stationary source [31] and becomes an emerging tool for damage identification. Several guided wave-based imaging studies have noted various types of defects such as cracks [32], corrosion [33], and impact damage [34] and applying conventional techniques for damage identification such as delay and sum imaging [35], minimum variance imaging [36], and the combination of both [37]. Flynn et al. describes a method of structural imaging through local wavenumber estimation of guided waves and carried out experiments producing images of hidden wall-thinning in an aluminum plate and a steel pipe to verify the method [38]. Yu et al. presented the guided wavefield analysis methods for damage detection in aluminum plate focusing the new wavenumber creation by wave changes at the structural anomaly, distinguished in the frequency-wavenumber spectra [39]. The iterative algebraic A_0-mode Lamb wave-based method has been used by Wang et al. to locate the corrosion damage at the edge of the cylindrical hole where hydrofluoric acid with a concentration of 20% was used to corrode the specimen artificially [40]. The interaction between Lamb waves with a notch perpendicular to the top surface of the thin plate examined by Alkassar et al. utilizes the mode conversion between S_0 and A_0-mode to detect the damage [41]. Weighted root mean square (WRMS) calculation from the recorded time series normal displacement due to Lamb wave propagation over a defected region capitalizes by Rucka et al. to identify the integrity of a joint by means of reconstructing the damage image [42]. Yelve et al. proposes a couple of Lamb wave-based new damage detection algorithms named as curve-intersection and sub-quadrant in thin aluminium plate [43].

This paper addresses a novel technique of guided ultrasonic wave imaging, independent of the local wavenumber. It describes the method to detect the defect in plate-like isotropic structure by accounting the linearity of the shear strain of the normal displacement on the surface. It introduces a graphical presentation that reconstructs the shape and size of the damage. The proposed technique can be summarized as follows: (a) acquiring time-based data of normal displacement at the upper surface, (b) determining the orthogonal set of normal shear strains (c) calculating the determinant of covariance matrix consists of above vector, (d) gathering the wave frontal image of the defected region. The proposed technique employs a non-contact laser vibrometer that are used to sequentially scan the displacement of the surface nodes. The proposed imaging technique evaluates and validates the robustness of the method for damage located under coating film in numerical and experimental case studies.

II. Analytical Model

With a phase velocity vector $\mathbf{V^i}$, and displacement component u_z^i, the 2D incoming wave equation of an A_0-mode Lamb wave field can be expressed as:

$$\frac{\partial^2 u_z^i}{\partial t^2} + (\mathbf{V}^i)^2 \nabla^2 u_z^i = 0 \tag{1}$$

Plane wave based decomposition returns

$$\left(\frac{\partial u_z^i}{\partial t} + V^{i\mathrm{T}} \nabla u_z^i\right)\left(\frac{\partial u_z^i}{\partial t} - V^{i\mathrm{T}} \nabla u_z^i\right) = 0 \tag{2}$$

The linearity condition within the advection equation can be termed as

$$\frac{\partial u_z^i}{\partial x} = -\frac{V_x^i}{(\mathbf{V}^i)^2}\frac{\partial u_z^i}{\partial t}, \qquad \frac{\partial u_z^i}{\partial y} = -\frac{V_y^i}{(\mathbf{V}^i)^2}\frac{\partial u_z^i}{\partial t} \tag{3}$$

This linearity condition only stands for existing the incoming wave field. For the cylindrical wave propagation, a covariance matrix with the combination of the out-of-plane shear strain vector can be assumed as:

$$\mathbb{C} = \begin{pmatrix} C_{11} & C_{12} \\ C_{21}^* & C_{22} \end{pmatrix} = \lim_{T\to\infty} \frac{1}{T} \int_0^T \nabla u_z (\nabla u_z)^T \mathrm{dt} \tag{4}$$

When the incident wave exist only

$$C_{11} = \frac{(v_x^i)^2}{(\mathbf{v}^i)^4}\Phi_{tt};\ C_{12} = C_{21} = \frac{v_x^i v_y^i}{(\mathbf{v}^i)^4}\Phi_{tt};\ C_{22} = \frac{(v_y^i)^2}{(\mathbf{v}^i)^4}\Phi_{tt}$$

$$\Phi_{tt} = \lim_{T\to\infty}\frac{1}{T}\int_0^T \frac{\partial u_z^i}{\partial t}\left(\frac{\partial u_z^i}{\partial t}\right)^{\dagger} \mathrm{dt}$$

As linearity condition maintains for the existing of the incident wave, the determinant of the covariance matrix becomes zero. Because of presence of the defect, the spatial gradient of the of the overlapped wave becomes

$$\frac{\partial u_z^{total}}{\partial x} = -\frac{V_x^i}{(\mathbf{V}^i)^2}\frac{\partial u_z^i}{\partial t} - \frac{V_x^s}{(\mathbf{V}^s)^2}\frac{\partial u_z^s}{\partial t},$$
$$\frac{\partial u_z^{total}}{\partial y} = -\frac{V_y^i}{(\mathbf{V}^i)^2}\frac{\partial u_z^i}{\partial t} - \frac{V_y^s}{(\mathbf{V}^s)^2}\frac{\partial u_z^s}{\partial t} \quad (5)$$

Determinant of the overlapped wave can be calculated as

$$|\mathbb{C}| = \begin{vmatrix} V_x^i & V_x^s \\ V_y^i & V_y^s \end{vmatrix}^2 \begin{vmatrix} \Phi_{t^i t^i} & \Phi_{t^i t^s} \\ \Phi_{t^s t^i} & \Phi_{t^s t^s} \end{vmatrix} \geq 0$$

Where,

$$\Phi_{t^i t^i} = \lim_{T\to\infty}\frac{1}{T}\int_0^T \frac{\partial u_z^i}{\partial t}\left(\frac{\partial u_z^i}{\partial t}\right)^{\dagger} \mathrm{dt}$$
$$\Phi_{t^s t^s} = \lim_{T\to\infty}\frac{1}{T}\int_0^T \frac{\partial u_z^s}{\partial t}\left(\frac{\partial u_z^s}{\partial t}\right)^{\dagger} \mathrm{dt}$$
$$\Phi_{t^i t^s} = \lim_{T\to\infty}\frac{1}{T}\int_0^T \frac{\partial u_z^i}{\partial t}\left(\frac{\partial u_z^s}{\partial t}\right)^{\dagger} \mathrm{dt}$$

It is predicted that, at the overlapping region, the linearity condition does not exist anymore and determinant of the adopted covariance matrix shows significant value. Assuming a 2D wave equation is likely to describe the normal displacement at the upper surface of the plate in a fundamental order antisymmetric mode Lamb wave field. Let us consider the near-field analysis of the scattering and transmitting object from a subsurface cylindrical defect. Fig. 1 depicts the geometrical relations between the incident plane wave and the cylinder.

The radius of the defect, a, assumed to be satisfied the condition as $2\pi a \ll \lambda_\mathrm{i}$, where λ_i denotes the incident wave's wavelength. The vector of the observation point and the scattering point on the edge of the cylindrical cavity can be denoted as:

$$\overrightarrow{OP} = \boldsymbol{r} = \begin{pmatrix} r\cos\phi \\ r\sin\phi \end{pmatrix}, \qquad \overrightarrow{OQ} = \boldsymbol{a} = \begin{pmatrix} a\cos\psi \\ a\sin\psi \end{pmatrix}$$

The normal vector at Q, $\boldsymbol{n}$, and the wave-number vector $\boldsymbol{k}$ can be denoted respectively as:

$$\boldsymbol{n} = \begin{pmatrix} \cos\psi \\ \sin\psi \end{pmatrix}, \quad \boldsymbol{k}_\mathrm{i} = \begin{pmatrix} k_\mathrm{i} \\ 0 \end{pmatrix} = \begin{pmatrix} 2\pi/\lambda_\mathrm{i} \\ 0 \end{pmatrix}$$

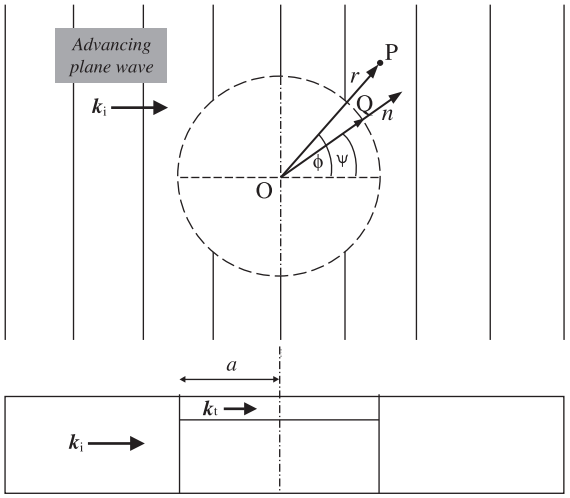

Fig. 1. Geometrical model of the defect, *a*: radius of the cylindrical cavity, $\boldsymbol{k}_\mathrm{i}$: incident wave-number vector.

Where ω is the angular frequency, v is the phase velocity of the plane wave. Within the low-frequency band, A_0 is the most dominant mode, and its phase velocity follows proportional behaviour with the product of frequency and plate-thickness. Incoming (incident) plane wave equation can be written as:

$$u_z^i(\boldsymbol{r}, t) = \mathrm{e}^{(\mathrm{i}\boldsymbol{k}_\mathrm{i}^\mathrm{T}\boldsymbol{r})}\mathrm{e}^{(-\mathrm{i}\omega t)} \quad (6)$$

Assuming that the transmitted waves are finite at the origin and the scattered waves take the form of outgoing cylindrical waves at infinity. It is considered that the perimeter of the cylindrical subsurface cavity is considerably smaller than the incident wavelength. On the basis of the above-mentioned considerations at the outside of the defect, the determinant can be given as [44]:

$$\begin{aligned} |\mathbb{C}| &\cong \frac{1}{4}\left(\frac{k_\mathrm{t}-k_\mathrm{i}}{k_\mathrm{t}+k_\mathrm{i}}\right)^2\left(\frac{2\pi}{r}\right)^2\left(\frac{k_\mathrm{i}a}{2}\right)^4 \sin^2\phi \\ &\cdot\left\{16k_\mathrm{i}^2\cos^2\phi\left|H_1^{(1)}(k_\mathrm{i}r)\right|^2 + k^4r^2\left|H_1^{(1)}(k_\mathrm{i}r)\right|^2\right. \\ &+ 4k_\mathrm{i}^2r^2\cos^2\phi\left|H_2^{(1)}(k_\mathrm{i}r)\right|^2 \\ &\left.+ 4\left(\frac{2\pi}{r}\right)^2\left(\frac{ka}{2}\right)^4 r^2\cos^2\phi\left|H_1^{(1)}(k_\mathrm{i}r)\right|^2\left|H_2^{(1)}(k_\mathrm{i}r)\right|^2\right\} \end{aligned} \quad (7)$$

The determinant of the matrix follows following features:

(i) $|\mathbb{C}| > 0$, when any inhomogeneity does exist along the path of the incident wave, i.e., at the linearity violation points.

(ii) The value of $|\mathbb{C}|$ concentrated significantly at the point of overlapping of the incident and scattered wave field region, i.e., near field of the subsurface defect. The distribution of $|\mathbb{C}|$ is further utilized for the imaging of defects.

III. Numerical Investigation

A. Finite Element Model

The objective of the numerical investigation is to investigate

the robustness of the proposed Lamb-wave-based corrosion detection under paint for isotropic plate-like structure. A 3D finite element method is employed to simulate the fundamental order anti-symmetric mode (A_0) Lamb wave propagating and scattering. Considering the elastic properties of the specimen to be interrogated in this study of $E = 205$ GPa, $\nu = 0.25$, and $\rho = 7800$ kg/m^3, theoretical Lamb wave dispersion curve for *S*45*C* material is depicted in Fig. 2.

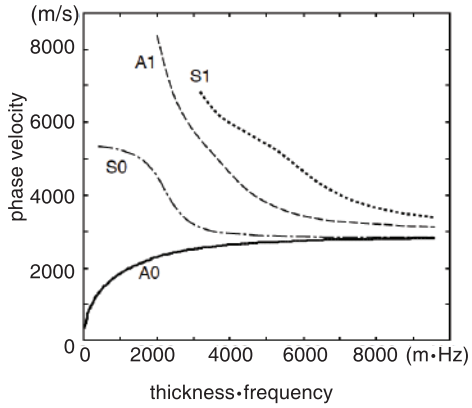

Fig. 2. Dispersion curves for anti-symmetric (*A*) and symmetric (*S*) modes in an S45C plate.

The multi-physics software LS-DYNA is used to generate the geometry and perform the meshing of the FE model [45]. A flawless plate is modelled using eight-noded 3D reduced integration solid brick elements. For the explicit type of finite difference numerical analysis, the spatial (Δx, Δy) and temporal (Δt) discretization is chosen as 0.15 mm, 0.15 mm, and 10 ns respectively, to satisfy the CFL condition [46]. A sample run is carried out to check the plane wave propagation behaviour in the isotropic body. To do so, a circular source of 0.3 mm diameter is excited with 30 kHz mono-cycle tone-burst from the centre of the plate. A contour of normal displacement of the particles taken into account and Fig. 3 demonstrates the Lamb wave propagating behaviour within the body.

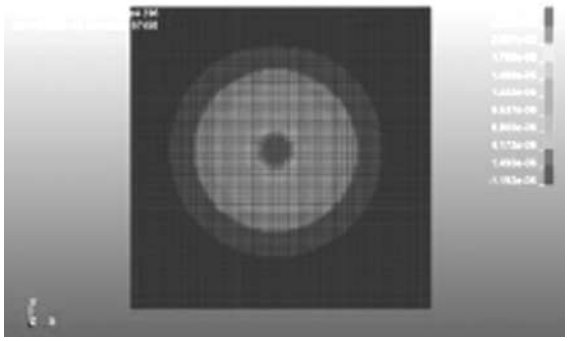

Fig. 3. Snapshot of the out-of-plane displacement of propagating Lamb wave at 9 μs for f=30 kHz

According to the phase velocity dispersion curve depicted in Figure 3 although the S_0-mode also exist at the low frequency-thickness regime, the applied normal nodal displacement generates too little horizontal in-plane motion. The geometry of the model with a subsurface artificial cylindrical small defect with the considered coordinate system is illustrated in Fig. 4.

The 2.3 mm thick plate with 1 mm height cylindrical defect placed 0.015 mm from the surface is modelled with the combination of using eight-noded solid brick elements and six-noded wedge elements. All planes of the specimen including the defected region satisfy the zero-strain conditions except the source plane. At the commencement of the investigation, a signal is applied to the vertical plane at "L" end of the 3D model as depicted in Fig. 5 and the wave is assumed to propagate along "R" end. For demonstration purpose, a series of normal displacement fields are shown in Fig. 5, to illustrate the Lamb wave propagation and scattering in the plate-like isotropic structure.

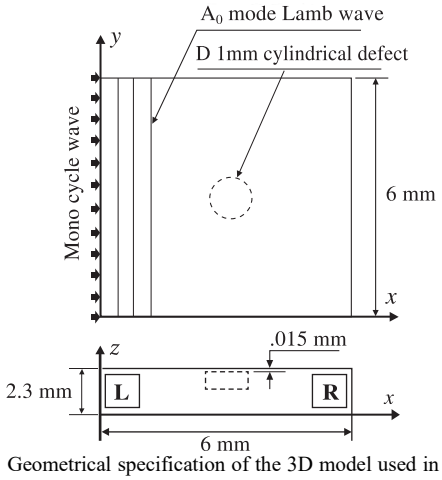

Fig. 4. Geometrical specification of the 3D model used in the finite element simulations

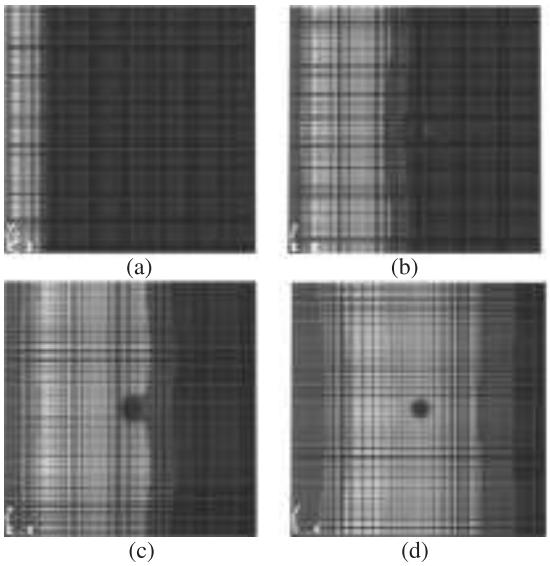

Fig. 5. Snapshots of normal displacement of propagating and scattered Lamb waves at (a) 3 μs, (b) 7 μs, (c) 11 μs, and, (d) 14 μs.

Small stiffness-weighted damping was considered to enhance the numerical stability and simulate the damping effect of the material. The hourglass energy was guaranteed less than 2% of the internal energy for all simulations which ensure the accurate prediction of the Lamb wave field. At the specified temporal interval, the normal displacement (z-directional DOF)

of the top surface particles is continuously monitored from the very beginning of the irradiation. Recorded time series displacement data further analyzed to reconstruct the image of the defect.

B. Data Analysis and Result

From the collected top surface nodal displacement data, dynamic shear strains are calculated by *Sobel* filter. This filtering technique utilizes two 5 × 5 kernels: one estimates the gradient in the x-direction, while the other estimates that in the y -direction (illustrates in Fig. 6) and formulated by:

$$f_x(x,y,t) = \sum_{\xi=-2}^{2}\sum_{\zeta=-2}^{2} S_{obelx}^{[5\times5]}(\xi,\zeta) \cdot f(x-\xi\Delta x, y-\zeta\Delta y, t) \quad (8)$$

$$f_y(x,y,t) = \sum_{\xi=-2}^{2}\sum_{\zeta=-2}^{2} S_{obely}^{[5\times5]}(\xi,\zeta) \cdot f(x-\xi\Delta x, y-\zeta\Delta y, t) \quad (9)$$

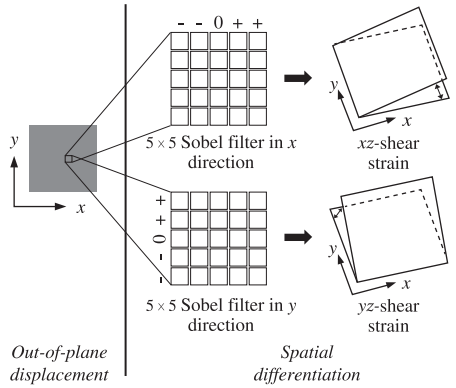

Fig. 6. Schematic of the *Sobel* filter to determine the orthogonal pair of spatial gradient.

The analysis concluded with the findings of each component of the covariance matrix using the following decaying series:

$$C_{xx} = \frac{1}{N\Delta t}\sum_{n=0}^{N} \alpha^n .\ f_x(x,y,(N-n)\Delta t) \cdot f_x(x,y,(N-n)\Delta t)\Delta t \quad (10)$$

Where α satisfies the following relation:

$$\alpha = e^{-\Delta t/r} \quad (11)$$

The time-constant, τ, controls the integral duration and it should be much longer than the period of the incident wave. Fig. 7 depicts the out-of-plane displacement distribution.

Due to the presence of a defect, the sinusoidal signal scattered from the boundary of the defect and overlap with the incident wave field. The energy of the overlapping region spatially concentrated in the vicinity of the source and not propagated. As described, because of overlapping incidence, the linearity of out-of-surface shear strains does not exist anymore. Accordingly, the determinant exhibits more significant value than zero. It is evident that at the periphery of the defect boundary, the determinant of the covariance matrix can figure out the points of violation of linearity and thus reconstructed the subsurface defect (Fig. 7 (b)).

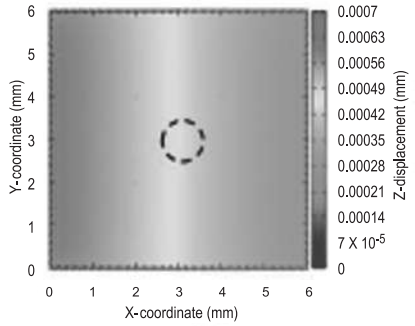

(a)

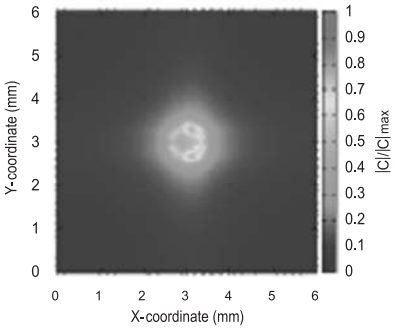

(b)

Fig. 7. Snapshot of (a) out-of-surface displacement and (b) distribution of normalized determinant after 14μs of irradiation for subsurface defected plate (dashed circle indicates the original position of artificial cylindrical defect).

IV. ACOUSTICAL EXPERIMENT

An acoustical experiment is conducted to provide the practical validation of the findings of the analytical and finite element model work. A 140 mm × 140 mm × 1 mm thick S45C plate is provided for the experiment. An aluminum film of 0.012 mm (Fig. 8) is used to cover the engraved region.

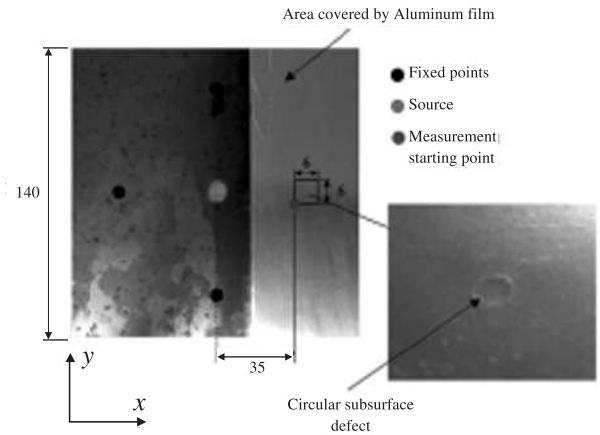

Fig. 8. Prepared specimen partly covered by the aluminum film (measurements are in mm).

Langevin transducer is used for wave excitation, and a micro-laser interferometer is used as the sensing tool. The entire experimental setup is shown in Fig. 9 (a). Fig. 9 (b) shows the exterior of the laser vibrometer. This interferometric probe can detect the out-of-plane displacement upto 0.08 nm in amplitude. The transducer is located at the centre of the plate (Figure 8) and is allowed to irradiate 30 kHz mono-cycle cylindrical wave. The ultrasonic wave propagated along the specimen, interacted with the defect and the laser vibrometer measured the out-of-plane response. The received response is then sampled transferred to a microcomputer for storage and further processing. The probe measures the out-of-plane displacement at the adjacent four points as, $f_1(x,y,t)$, $f_2(x,y,t)$, $f_3(x,y,t)$, and $f_4(x,y,t)$. The shear strains are obtained as follows:

$$f_x(x,y,t) = \frac{f_1(x,y,t) - f_3(x,y,t)}{\Delta x} \qquad (12)$$
$$f_y(x,y,t) = \frac{f_2(x,y,t) - f_4(x,y,t)}{\Delta y}$$

Here, Δx and Δy are denoted the x and y directional sampling interval (0.5 mm) respectively.

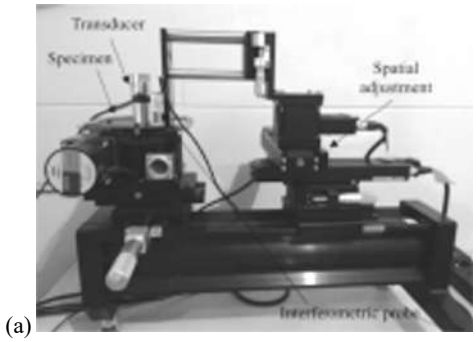

(a)

(b)

Fig. 9. (a) Experimental setup for the measurement of Lamb waves, (b) An exterior view of the micro laser interferometer (MLI-80).

These shear strains further utilize to calculate each component of the covariance matrix, consequently the determinant. Fig. 10 (left) shows the view of the normalized vertical displacement of the surface particle. The corresponding snapshot, Fig. 10(right), shows the reconstructed image of the subsurface defect obtained by the proposed dynamic shear strain analysis. As a result, the proposed method can figure out the subsurface cylindrical defect which is smaller than the incident wavelength of 24 mm.

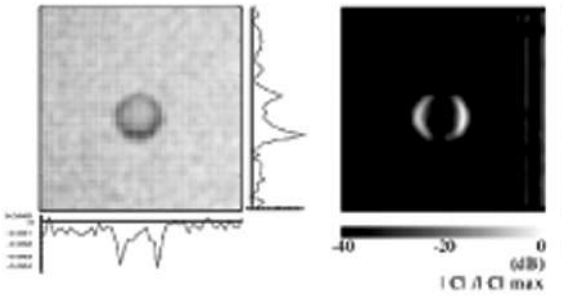

Fig. 10. Snapshot of (left) normalized out-of-plane displacement and (right) the normalized determinant of the covariance, normalized by the maximum value, $|\mathbb{C}|_{\max}$.

V. CONCLUSION

In this study, the dynamic shear strain analysis for reconstructing a silhouette of the corroded region in the paint-coated metallic structure is proposed using the linearity among the orthogonal pair of the out-of-plane shear strains. By analyzing the shear strains vector, it can be said that the determinant of the proposed covariance matrix concentrates its energy inside the near-field of the scattered cylindrical waves. The methods are numerically implemented in the defected 3D model to show the characteristics of the determinant of the adopted covariance matrix. In the experiment, Langevin transducer is employed to excite A_0-mode lamb wave. A laser interferometer is used to capture the out-of-plane displacement. Comparing the results of analytical prediction, numerical simulation, and experimental measurement, it can be seen that the proposed method efficiently detects the corrosion under paint in the form of an image of the defected region. Thus, it is also proved that A_0-mode is suitable for SHM in metallic structure. Further studies will apply to assess the effectiveness of this proposed Lamb wave based through-hole cylindrical damage detection method in CFRP laminates. Furthermore, the current study has been developed on the incident of a single plane wave. A wavelet-based analysis can also be studied to interrogate the composite.

REFERENCES

[1] Lowe, M. J. (1995). Matrix techniques for modeling ultrasonic waves in multilayered media. *IEEE transactions on ultrasonics, ferroelectrics, and frequency control*, *42*(4), 525-542.

[2] Chimenti, D. E. (1997). Guided waves in plates and their use in materials characterization. *Applied Mechanics Reviews*, *50*(5), 247-284.

[3] Worlton, D. C. (1961). Experimental confirmation of Lamb waves at megacycle frequencies. *Journal of Applied Physics*, *32*(6), 967-971.

[4] Viktrov, I. A. (1967). Rayleigh and Lamb waves: physical theory and applications. *Chapter II*.

[5] Mansfield, T. L. (1975). Lamb wave inspection of aluminum sheet. *Materials evaluation*, *33*(4).

[6] Rokhlin, S. I. (1981). Resonance phenomena of Lamb waves scattering by a finite crack in a solid layer. *The Journal of the Acoustical Society of America*, *69*(4), 922-928.

[7] Paffenholz, J., Fox, J. W., Gu, X., Jewett, G. S., Datta, S. K., & Spetzler, H. A. (1990). Experimental and theoretical study of Rayleigh-Lamb waves in a plate containing a surface-breaking crack. *Research in Nondestructive Evaluation*, *1*(4), 197-217.
[8] Alleyne, D. N., & Cawley, P. (1992). The interaction of Lamb waves with defects. *IEEE transactions on ultrasonics, ferroelectrics, and frequency control*, *39*(3), 381-397.
[9] Wilcox, P., Lowe, M., & Cawley, P. (2001). The effect of dispersion on long-range inspection using ultrasonic guided waves. *NDT & E International*, *34*(1), 1-9.
[10] Pierce, S. G., Culshaw, B., Manson, G., Worden, K., & Staszewski, W. J. (2000, June). Application of ultrasonic Lamb wave techniques to the evaluation of advanced composite structures. In *Smart Structures and Materials 2000: Sensory Phenomena and Measurement Instrumentation for Smart Structures and Materials* (Vol. 3986, pp. 93-103). International Society for Optics and Photonics.
[11] Lemistre, M., & Balageas, D. (2001). Structural health monitoring system based on diffracted Lamb wave analysis by multiresolution processing. *Smart materials and structures*, *10*(3), 504.
[12] Terrien, N., Osmont, D., Royer, D., Lepoutre, F., & Déom, A. (2007). A combined finite element and modal decomposition method to study the interaction of Lamb modes with micro-defects. *Ultrasonics*, *46*(1), 74-88.
[13] Roh, Y. S., & Chang, F. K. (1995). Effect of impact damage on Lamb wave propagation in laminated composites. *Dynamic response and behavior of composites*, 127-138.
[14] Greve, D. W., Zheng, P., & Oppenheim, I. J. (2008). The transition from Lamb waves to longitudinal waves in plates. *Smart materials and structures*, *17*(3), 035029.
[15] Pei, J., Yousuf, M. I., Degertekin, F. L., Honein, B. V., & Khuri-Yakub, B. T. (1996). Lamb wave tomography and its application in pipe erosion/corrosion monitoring. *Journal of Research in Nondestructive Evaluation*, *8*(4), 189-197.
[16] Monkhouse, R. S. C., Wilcox, P. W., Lowe, M. J. S., Dalton, R. P., & Cawley, P. (2000). The rapid monitoring of structures using interdigital Lamb wave transducers. *Smart Materials and Structures*, *9*(3), 304.
[17] Kessler, S. S., Spearing, S. M., & Soutis, C. (2002). Damage detection in composite materials using Lamb wave methods. *Smart materials and structures*, *11*(2), 269.
[18] Grondel, S., Paget, C., Delebarre, C., Assaad, J., & Levin, K. (2002). Design of optimal configuration for generating A0 Lamb mode in a composite plate using piezoceramic transducers. *The Journal of the Acoustical Society of America*, *112*(1), 84-90.
[19] Belanger, P., & Cawley, P. (2009). Feasibility of low frequency straight-ray guided wave tomography. *NDT & E International*, *42*(2), 113-119.
[20] Hughes, D., Wang, N., Case, T., Donnell, K., Zoughi, R., Austin, R., & Novack, M. (2001). Microwave nondestructive detection of corrosion under thin paint and primer in aluminum panels. *Subsurface Sensing Technologies and Applications*, *2*(4), 435-471.
[21] Sargent, J. P. (2011, October). Corrosion and crack detection in metal plates using Lamb waves. In *6th NDT in Progress, International Workshop of NDT Experts, Prague*.
[22] Sargent, J. P. (2006). Corrosion detection in welds and heat-affected zones using ultrasonic Lamb waves. *Insight-Non-Destructive Testing and Condition Monitoring*, *48*(3), 160-167.
[23] J. P. Sargent. NDT and SHM of welds and heat affected zones using weld guided Lamb waves.
[24] Anastasi, R. F., & Madaras, E. I. (2006, March). Terahertz NDE for under paint corrosion detection and evaluation. In *AIP Conference Proceedings* (Vol. 820, No. 1, pp. 515-522). AIP.
[25] Diamond, G. G., Kubasiak, P., Kyeyune, K. P., Wootton, A. M., & Bishop, C. (2014). Remote detection of corrosion under paint (CUP) from distances greater than 5 metres. *Proceedings of the 11th ECNDT*.
[26] Yu, L., Giurgiutiu, V., Wang, J., & Shin, Y. J. (2012). Corrosion detection with piezoelectric wafer active sensors using pitch-catch waves and cross-time–frequency analysis. *Structural Health Monitoring*, *11*(1), 83-93.
[27] Rathod, V. T., & Mahapatra, D. R. (2011). Ultrasonic Lamb wave based monitoring of corrosion type of damage in plate using a circular array of piezoelectric transducers. *NDT & E International*, *44*(7), 628-636.
[28] Nagy, P. B., Simonetti, F., & Instanes, G. (2014). Corrosion and erosion monitoring in plates and pipes using constant group velocity Lamb wave inspection. *Ultrasonics*, *54*(7), 1832-1841.
[29] Chew, D., & Fromme, P. (2015, March). Monitoring of corrosion damage using high-frequency guided ultrasonic waves. In *AIP Conference Proceedings* (Vol. 1650, No. 1, pp. 777-784). AIP Publishing..
[30] Sharma, S., & Mukherjee, A. (2015). Ultrasonic guided waves for monitoring corrosion in submerged plates. *Structural Control and Health Monitoring*, *22*(1), 19-35.
[31] Michaels, J. E. (2017, February). Ultrasonic wavefield imaging: Research tool or emerging NDE method?. In *AIP Conference Proceedings* (Vol. 1806, No. 1, p. 020001). AIP Publishing.
[32] Michaels, T. E., Michaels, J. E., & Ruzzene, M. (2011). Detection and sizing of subsurface impedance discontinuities using acoustic wavefield images. In *Proceedings of the 8th International Workshop on Structural Health Monitoring* (pp. 2215-2222). DEStech Publications, Inc., Lancaster, PA.
[33] Michaels, T. E., & Michaels, J. E. (2007, April). Monitoring and characterizing corrosion in aluminum using Lamb waves and attached sensors. In *Health Monitoring of Structural and Biological Systems 2007* (Vol. 6532, p. 65321G). International Society for Optics and Photonics.
[34] Sohn, H., Dutta, D., Yang, J. Y., DeSimio, M., Olson, S., & Swenson, E. (2011). Automated detection of delamination and disbond from wavefield images obtained using a scanning laser vibrometer. *Smart Materials and Structures*, *20*(4), 045017.
[35] Chen, X., Michaels, J. E., Lee, S. J., & Michaels, T. E. (2012). Load-differential imaging for detection and localization of fatigue cracks using Lamb waves. *Ndt & E International*, *51*, 142-149.
[36] Hall, J. S., & Michaels, J. E. (2010). Minimum variance ultrasonic imaging applied to an in situ sparse guided wave array. *IEEE transactions on ultrasonics, ferroelectrics, and frequency control*, *57*(10), 2311-2323.
[37] Hall, J. S., Fromme, P., & Michaels, J. E. (2011). Ultrasonic guided wave imaging for damage characterization.
[38] Flynn, E. B., Chong, S. Y., Jarmer, G. J., & Lee, J. R. (2013). Structural imaging through local wavenumber estimation of guided waves. *Ndt & E International*, *59*, 1-10.
[39] Yu, L., Tian, Z., & Leckey, C. A. (2015). Crack imaging and quantification in aluminum plates with guided wave wavenumber analysis methods. *Ultrasonics*, *62*, 203-212.
[40] Wang, D., Zhang, W., Wang, X., & Sun, B. (2016). Lamb-wave-based tomographic imaging techniques for

hole-edge corrosion monitoring in plate structures. *Materials*, *9*(11), 916.
[41] Alkassar, Y., Agarwal, V. K., & Alshrihi, E. (2017). Simulation of Lamb Wave Modes Conversions in a Thin Plate for Damage Detection. *Procedia Engineering*, *173*, 948-955.
[42] Rucka, M., Wojtczak, E., & Lachowicz, J. (2018). Damage imaging in Lamb wave-based inspection of adhesive joints. *Applied Sciences*, *8*(4), 522.
[43] Yelve, N. P., Rode, S., Das, P., & Khanolkar, P. (2019). Some new algorithms for locating a damage in thin plates using lamb waves. *Engineering Research Express*, *1*(1), 015027.
[44] Teramoto, K., & Sanaul, R. M. Image Reconstruction of Corrosion under Coating Film by Dynamic Shear Strain Analysis of Lamb Waves, *Proceedings of the 19th WCNDT*.
[45] Manual, LS-DYNA Keyword User'S., and I. Volume. (2007). Version 971. *Livermore Software Technology Corporation* 7374.
[46] Courant, R., Friedrichs, K., & Lewy, H. (1967). On the partial difference equations of mathematical physics. *IBM journal of Research and Development*, *11*(2), 215-234.

M S Rabbi was born in Rangpur city, Bangladesh, in 1985. He received the B.Sc. and M.Sc. degrees in Mechanical engineering from the Chittagong University of Engineering and Technology, Chattogram, in 2008 and 2013 respectively. He has done the Ph.D. degree in NDT from Saga University, Japan, in 2008, From 2017 to 2018, Mr. Rabbi was a visiting researcher with the Ultrasonic Laboratory. Since 2008, he has been a faculty member with the Mechanical Engineering Department, Chittagong University of Engineering and Technology. His research interests include non-destructive evaluation & testing, composite materials, and structural health monitoring.

Prof. K. Teramoto received the B.Sc. Engg. degree in instrumentation physics and mathematical engineering from Tokyo University, Japan in 1983, and the M.Sc. Engg. degree from the same institution in 1985. He has completed his Ph.D. from Tokyo University in 1988
His research interest includes inverse problem, acoustical sensing, acoustical signal processing acoustical imaging, image and signal reconstruction, nonlinear optimization. Prof. Teramoto is the member of Institute of Electrical and Electronics Engineers (IEEE), Signal Processing Society, and UFFC, Society of Instrument and Control Engineers (SICE), Acoustic Society of Japan.